POLITECNICO DI TORINO
Repository ISTITUZIONALE

Multi-Valley Superconductivity in Ion-Gated MoS2 Layers

(Article begins on next page)

25 April 2024

Multi-Valley Superconductivity In Ion-Gated MoS$_2$ Layers

Erik Piatti,[1, *] Domenico De Fazio,[2, *] Dario Daghero,[1] Srinivasa Reddy
Tamalampudi,[2] Duhee Yoon,[2] Andrea C. Ferrari,[2] and Renato S. Gonnelli[1]

[1] *Department of Applied Science and Technology, Politecnico di Torino, 10129 Torino, Italy*
[2] *Cambridge Graphene Centre, University of Cambridge, Cambridge CB3 OFA, UK*

Layers of transition metal dichalcogenides (TMDs) combine the enhanced effects of correlations associated with the two-dimensional limit with electrostatic control over their phase transitions by means of an electric field. Several semiconducting TMDs, such as MoS$_2$, develop superconductivity (SC) at their surface when doped with an electrostatic field, but the mechanism is still debated. It is often assumed that Cooper pairs reside only in the two electron pockets at the K/K' points of the Brillouin Zone. However, experimental and theoretical results suggest that a multi-valley Fermi surface (FS) is associated with the SC state, involving 6 electron pockets at the Q/Q' points. Here, we perform low-temperature transport measurements in ion-gated MoS$_2$ flakes. We show that a fully multi-valley FS is associated with the SC onset. The Q/Q' valleys fill for doping$\gtrsim 2 \cdot 10^{13}$cm^{-2}, and the SC transition does not appear until the Fermi level crosses both spin-orbit split sub-bands Q$_1$ and Q$_2$. The SC state is associated with the FS connectivity and promoted by a Lifshitz transition due to the simultaneous population of multiple electron pockets. This FS topology will serve as a guideline in the quest for new superconductors.

Keywords: Transition metal dichalcogenides, ionic gating, superconductivity, electron-phonon coupling, Raman spectroscopy, Lifshitz transitions

Transition metal dichalcogenides (TMDs) are layered materials with a range of electronic properties. Depending on chemical composition, crystalline structure, number of layers (N), doping, and strain, different TMDs can be semiconducting, metallic and superconducting[1]. Amongst semiconducting TMDs, MoS$_2$, MoSe$_2$, WS$_2$ and WSe$_2$ have sizeable bandgaps in the range$\sim$1-2eV[2]. When exfoliated from bulk to single layer (1L), they undergo an indirect-to-direct gap transition[2–4], offering a platform for electronic and optoelectronic applications[1,2,5], such as transistors[6–8], photodetectors[9–12], modulators[13] and electroluminescent devices[14,15].

For all TMDs with 2H crystal structure, the hexagonal Brillouin Zone (BZ) features high-symmetry points Γ, M, K and K'[4,16], Fig.1a. The minima of the conduction band fall at K, K', as well as at Q, Q', approximately half-way along the Γ-K(K') directions[4,16], Fig.1a. In absence of an out-of-plane electric field, the relative position of Q and Q' depends on N and strain[4,16,17]. The global minimum of the conduction band sits at K/K' in 1L-MoS$_2$ and at Q/Q' in few layer (FL)-MoS$_2$ with N$\geq$4[4]. When an electric field is applied perpendicular to the MoS$_2$ plane, inversion symmetry is broken and the global minimum of the conduction band is shifted to K/K' in any FL-MoS$_2$[16], Figs.1b-d. The valleys at K/K' and at Q/Q' are characterized by a different electron-phonon coupling (EPC)[18] and, when inversion symmetry is broken, by a different spin-orbit coupling (SOC)[19]. In particular, both EPC and SOC are larger in the Q/Q' valleys[18,19].

The field-effect transistor (FET) architecture is ideally suited to control the electronic properties of 1L flakes, as it simultaneously provides an electrostatic control of the transverse electric field and the carrier density. In the electric-double-layer (EDL) technique[20], the standard solid gate dielectric is replaced by an ionic medium, such as an ionic liquid or electrolyte. In this configuration, the EDL that forms at the ionic liquid/electrode interfaces supports electric fields in excess of$\sim$10MV/cm[21], corresponding to surface carrier densities $n_{2d} \gtrsim 10^{14}$cm^{-2}[21]. Ionic-liquid gating has been used to tune the Fermi level, E_F, in TMDs and explore transport at different carrier concentrations[22–26]. The vibrational properties of TMDs can also be controlled by means of the EDL technique, as suggested by gate-induced softening of Raman-active modes in 1L-MoS$_2$[27], while the opposite is observed in gated 1L[28] and two-layer (2L)[29] graphene. Ref. 23 reported a gate-induced superconducting state at the surface of liquid-gated MoS$_2$ flakes with N$\gtrsim$25[23], while Ref. 30 detected this down to N=1.

Most of these results have been interpreted in terms of the population of the conduction band minima at K/K'[23,31–33], which are global minima in both 1L-MoS$_2$[3,18] and electrostatically-doped FL-MoS$_2$[16,23,31,32], Fig.1b. Theoretical investigations however suggested that the population of the high-energy minima at Q/Q' may have an important role in determining the properties of gated MoS$_2$ flakes, by providing contributions both to EPC[16,18] and SOC[19,34]. Ref. 18 predicted that when the Q/Q' valleys of 1L-MoS$_2$ are populated (Fig.1c,d), EPC strongly increases (from$\sim$ 0.1 to$\sim$ 18), leading to a superconducting transition temperature $T_c \sim$ 20K for a doping level $x = 0.18$ electrons(e$^-$)/unit cell (corresponding to $E_F = 0.18 \pm 0.02$eV at K/K' and 0.08 ± 0.02eV at Q/Q')[16]. However, Ref. 30 measured $T_c \sim$ 2K for $x \sim 0.09 \div 0.17$ e$^-$/unit cell in e$^-$-doped 1L-MoS$_2$. This mismatch may be associated with the contribution of e$^-$– e$^-$ interactions, whose role in the determination of T_c is still under debate[35,36]. Overall, the agreement between the model of Ref. 18 and the trend of T_c with e$^-$ doping in Ref. 23 suggests that the mechanism of Ref. 18 for EPC enhancement when the Q/Q' valleys are crossed
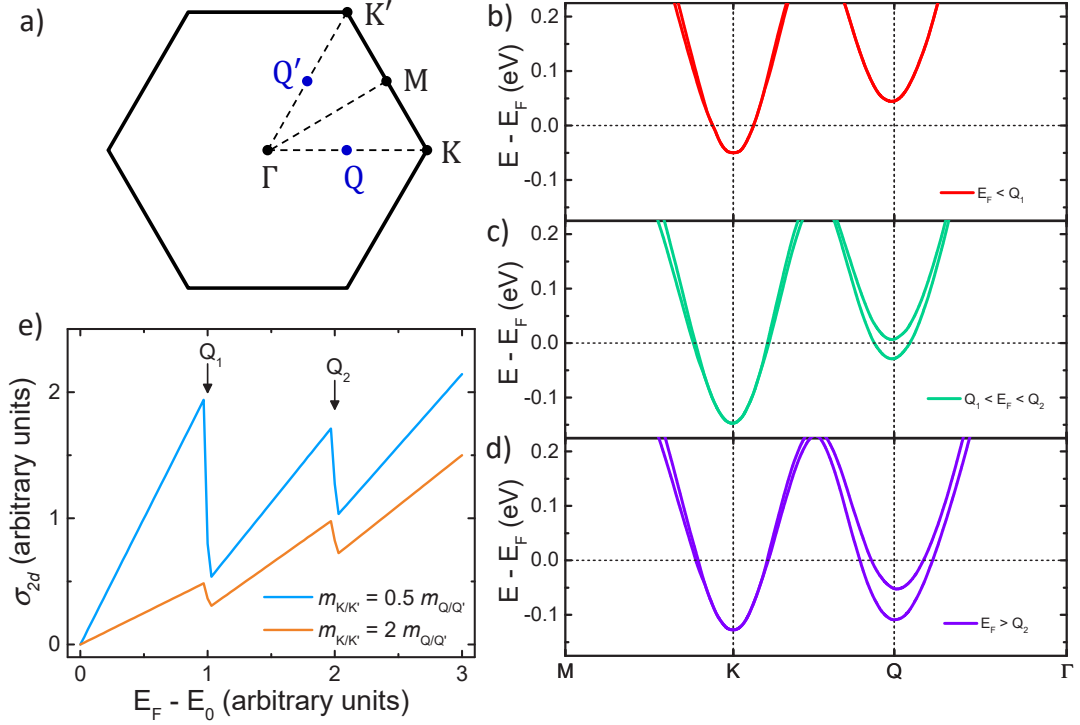
FIG. 1. a) BZ for the 2H crystal structure. High symmetry points Γ, M, K, K', and points Q and Q' are indicated. b-d) 3L-MoS_2 band structure for 3 doping values. The bands are adapted from Ref. 16, and were obtained by Density Functional Theory (DFT) calculations using the Quantum ESPRESSO package[86] in the field-effect transistor configuration[87]. The valleys at K/K' have two spin-orbit split sub-bands, with splitting much smaller than at Q/Q', not seen in this scale. e) Schematic dependence of σ_{2d} for increasing E_F above the global energy minimum of the conduction band, E_0, at T=0, for 2 ratios of the effective masses in the K/K' and Q/Q' electron pockets ($m_{K/K'}$ and $m_{Q/Q'}$). Curves are calculated using Eq.6 of Ref. 46 and setting a total degeneracy of 4 for the K/K' pockets, 6 for the first Q/Q' pocket (Q_1), and 6 for the second Q/Q' pocket (Q_2); physical constants and energy separations are set to unity.

may also hold for FL-MoS_2.

Inversion symmetry can be broken in MoS_2 either by going to the 1L limit[18], or by applying a transverse electric field[37,38]. This leads to a finite SOC[37,38], which lifts the spin degeneracy in the conduction band and gives rise to two spin-orbit-split sub-bands in each valley[16,37], as shown in Fig.1b-d for FL-MoS_2. When the system is field-effect doped, the inversion symmetry breaking increases with increasing transverse electric field[31,33], due to the fact that induced e^- tend to become more localized within the first layer[31,33,35]. Hence, the SOC and the spin-orbit splitting between the bands increase as well, as was calculated in Ref. 16.

When combined to the gate-induced SC state[38], this can give rise to interesting physics, such as spin-valley locking of the Cooper pairs[32] and 2d Ising superconductivity (SC)[31] with a non-BCS-like energy gap[39], suggested to host topologically non-trivial SC states[35,40,41]. Refs. 16,19 predicted SOC and spin-orbit splitting between sub-bands to be significantly stronger for the Q/Q' valleys than for K/K', thus supporting spin-valley locking at Q/Q' as well[34]. A dominant contribution of the Q/Q' valleys in the development of the SC state would be consistent with the high ($\gtrsim$ 50T) in-plane upper critical

field, $H_{c2}^{\parallel}$, observed in ion-gated MoS_2[31,32] and WS_2[42]. The $H_{c2}^{\parallel}$ enhancement is caused by locking of the spin of the Cooper pairs in the out-of-plane direction in a 2d superconductor in the presence of finite SOC, and is therefore promoted by increasing the SOC. However, $H_{c2}^{\parallel}$ for MoS_2 and WS_2 is higher than in metallic TMD Ising superconductors (such as $NbSe_2$ and TaS_2), where $H_{c2}^{\parallel} \lesssim$ 30T[43], despite the SOC in the K/K' valleys being much smaller ($\sim$ 3meV for MoS_2[37]). Spin-valley locking in the Q/Q' valleys may thus explain this apparent inconsistency in the physics of ion-gated semiconducting TMDs under magnetic field.

From the experimental point of view, the possible multi-valley character of transport in gated TMDs is currently debated. Refs. 33,34,44 measured the Landau-level degeneracy at moderate $n_{2d} \sim 10^{12} - 10^{13} cm^{-2}$, finding it compatible with a carrier population in the Q/Q' valleys. However, Ref. 33 argued that this would be suppressed for larger $n_{2d} \gtrsim 10^{13} cm^{-2}$, typical of ion-gated devices and mandatory for the emergence of SC) due to stronger confinement within the first layer[33]. In contrast, angle-resolved photoemission spectroscopy in surface-Rb-doped TMDs[45] highlighted the presence of a

non-negligible spectral weight at the Q/Q' valleys only for $n_{2d} \gtrsim 8 \cdot 10^{13}$cm^{-2} in the case of MoS$_2$. Thus, which valleys and sub-bands are involved in the gate-induced SC state still demands a satisfactory answer.

Here we report multi-valley transport and SC at the surface of liquid-gated FL-MoS$_2$. We use a dual-gate geometry to tune doping across a wide range of $n_{2d} \sim 5 \cdot 10^{12} - 1 \cdot 10^{14}$cm^{-2}, induce SC, and detect characteristic "kinks" in the transconductance. These are non-monotonic features that emerge in the n_{2d}-dependence of the low-temperature (T) conductivity when E_F crosses the high-energy sub-bands[46], irrespectively of their specific effective masses, Fig.1e. We show that the population of the Q/Q' valleys is fundamental for the emergence of SC. The crossing of the first sub-band Q$_1$ (Fig.1c) occurs at small $n_{2d} \lesssim 2 \cdot 10^{13}$cm^{-2}, implying that multi-valley transport already occurs in the metallic phase over a wide range of $n_{2d} \sim 2 - 6 \cdot 10^{13}$cm^{-2}. We also show that the crossing of the second sub-band Q$_2$ occurs after a finite T_c is observed, while a full population of both spin-orbit-split sub-bands (Fig.1d) in the Q/Q' valleys is required to reach the maximum T_c. These results highlight how SC can be enhanced in MoS$_2$ by optimizing the connectivity of its Fermi Surface (FS), i.e. by adding extra FSs in different BZ regions to provide coupling to further phonon branches[47]. Since the evolution of the band structure of MoS$_2$ with field-effect doping is analogous to that of other semiconducting TMDs[16,34,36,45,46], a similar mechanism is likely associated with the emergence of SC in TMDs in general. Thus, optimization of the FS connectivity can be a viable strategy in the search of new superconductors.

We study flakes with N=4-10, as Refs. 4,16,46 predicted that flakes with N≥4 are representative of the bulk electronic structure, and Ref. 30 experimentally observed that both T_c and the critical magnetic field H_{c2} in 4L flakes are similar to those of 6L and bulk flakes. Our devices are thus comparable with those in literature[23,30–32,48]. We do not consider 1L flakes as they exhibit a lower T_c and their mobility is suppressed due to disorder[30,48].

FL-MoS$_2$ flakes are prepared by micro-mechanical cleavage[49] of 2H-MoS$_2$ crystals from SPI Supplies. The 2H phase is selected to match that in previous reports of gate-induced SC[23,30]. Low resistivity ($< 0.005\Omega\cdot$cm) Si coated with a thermal oxide SiO$_2$ is chosen as a substrate. We tested both 90 or 285nm SiO$_2$ obtaining identical SC results. Thus, 90nm SiO$_2$ is used to minimize the back gate voltage V_{BG} (-30V$< V_{BG} <$30V), while 285nm is used to minimize leakage currents through the back gate I_{BG}. Both SiO$_2$ thicknesses provide optical contrast at visible wavelengths[50]. A combination of optical contrast, Raman spectroscopy and atomic force microscopy (AFM) is used to select the flakes and determine N.

Electrodes are then defined by patterning the contacts area by e-beam lithography, followed by Ti:10nm/Au:50nm evaporation and lift-off. Ti is used as an adhesion layer[51], while the thicker Au layer
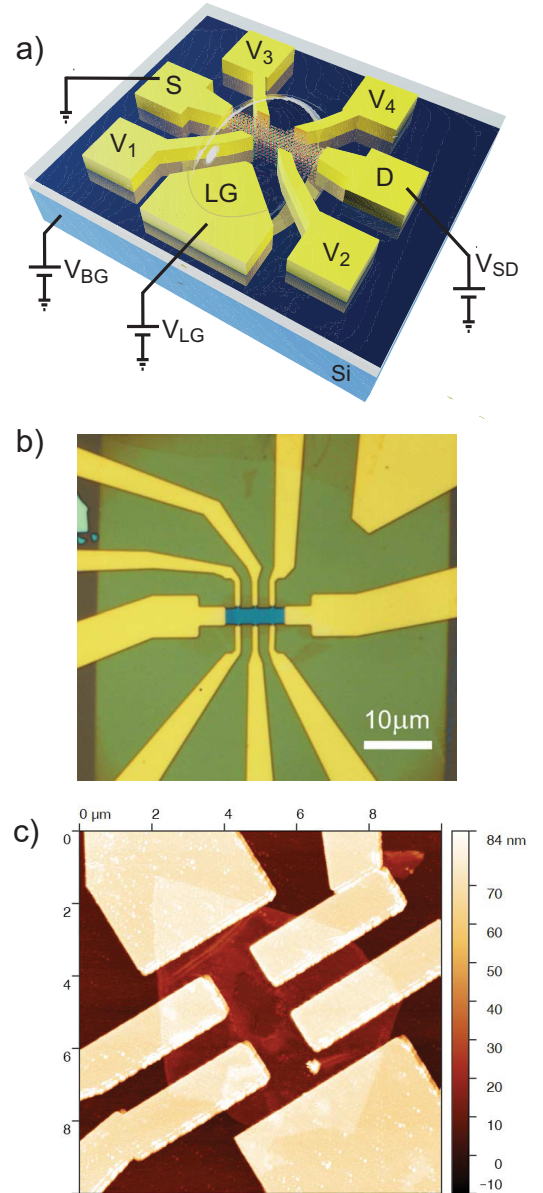

FIG. 2. a) Hall bar FL-MoS$_2$ flake with voltage probes (V_i), source (S), drain (D) and liquid-gate (LG) electrodes. A ionic liquid droplet covers the flake and part of the LG electrode. The sample is biased with a source-drain voltage (V_{SD}) and dual gate control is enabled by a voltage applied on the liquid gate (V_{LG}) and on the solid back gate (V_{BG}). b) Optical image of Hall bar with six voltage probes. The LG electrode is on the upper-right corner. c) AFM scan of the MoS$_2$ Hall bar after ionic liquid removal.

provides the electrical contact. Flakes with irregular shapes are further patterned in the shape of Hall bars by using polymethyl methacrylate (PMMA) as a mask and removing the unprotected MoS$_2$ with reactive ion etching (RIE) in a 150mTorr atmosphere of CF$_4$:O$_2$=5:1, as shown in Figs.2a,b. A droplet of 1-Butyl-1-methylpiperidinium bis(trifluoromethylsulfonyl)imide (BMPPD-TFSI) is used to cover the FL-MoS$_2$ surface
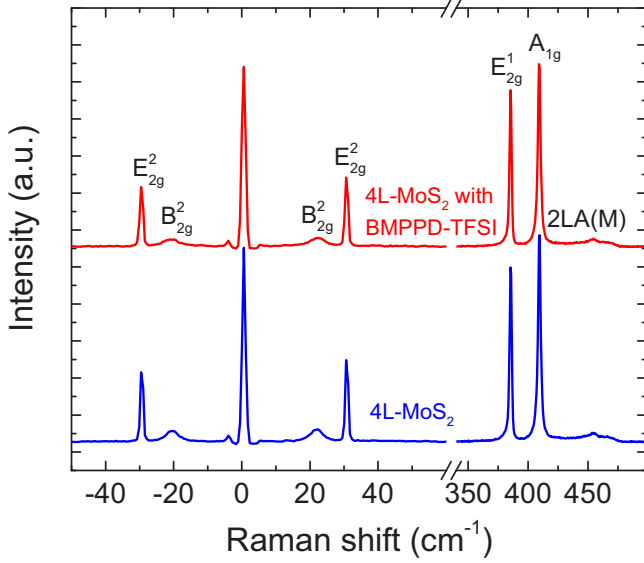
FIG. 3. Representative Raman spectra at 514nm of a 4L-MoS$_2$ flake before (blue) and after (red) device fabrication, deposition of the ionic liquid droplet and low-T transport measurements.

and part of the side electrode for liquid gate operation (LG), as sketched in Fig.2a.

AFM analysis is performed with a Bruker Dimension Icon in tapping mode. The scan in Fig.2c is done after the low-T experiments and removal of the ionic liquid, and confirms that the FL-MoS$_2$ sample does not show topographic damage after the measurement cycle.

We use Raman spectroscopy to characterize the devices both before and after fabrication and BMPPD-TFSI deposition. Raman measurements are performed with a Horiba LabRAM Evolution at 514nm, with a 1800grooves/mm grating and a spectral resolution$\sim$0.45cm^{-1}. The power is kept below 300μW to avoid any damage. A representative Raman spectrum of 4L-MoS$_2$ is shown in Fig.3 (blue curve). The peak at$\sim$455cm^{-1} is due to a second-order longitudinal acoustic mode at the M point[52]. The E$_{2g}^1$ peak at$\sim$385cm^{-1} and the A$_{1g}$ at$\sim$409cm^{-1} correspond to in-plane and out-of plane vibrations of Mo and S atoms[53,54]. Their difference, Pos(E$_{2g}^1$)-Pos(A$_{1g}$), is often used to monitor N[55]. However, for N$\geq$4, the variation in Pos(E$_{2g}^1$)-Pos(A$_{1g}$) between N and N+1 approaches the instrument resolution[55] and this method is no longer reliable. Thus, we use the low frequency modes (< 100cm^{-1}) to monitor N[56,57]. The shear (C) and layer breathing modes (LBM) are due to the relative motions of the atomic planes, either perpendicular or parallel to their normal[56]. Pos(C) and Pos(LBM) change with N as[56,57]:

$$\text{Pos(C)}_N = \frac{1}{\sqrt{2}\pi c}\sqrt{\frac{\alpha_\parallel}{\mu_m}}\sqrt{1 + \cos\left(\frac{\pi}{N}\right)} \quad (1)$$

$$\text{Pos(LBM)}_N = \frac{1}{\sqrt{2}\pi c}\sqrt{\frac{\alpha_\perp}{\mu_m}}\sqrt{1 - \cos\left(\frac{\pi}{N}\right)} \quad (2)$$

where $\alpha_\parallel \sim 2.82 \cdot 10^{19}$N/m^3 and $\alpha_\perp \sim 8.90 \cdot 10^{19}$N/m^3 are spring constants for C and LBM modes, respectively, c is the speed of light in vacuum, $\mu_m \sim 3 \cdot 10^{-6}$Kg/m^2 is the 1L mass per unit area[56,57]. Fig.3 shows a C mode at$\sim$30cm^{-1} and an LBM at$\sim$22cm^{-1}. These correspond to N=4 using Eqs.1,2. Fig.3 also plots the Raman measurements after device fabrication, deposition of the ionic liquid, low-T measurements, V_{LG} removal and warm-up to room T (red curve). We still find Pos(C)$\sim$30cm^{-1} and Pos(LBM)$\sim$22cm^{-1}, the same as those of the pristine flake, suggesting no damage nor residual doping.

Four-probe resistance and Hall measurements are then performed in the vacuum chambers of either a Cryomech pulse-tube cryocooler, T_{min}=2.7K, or a Lakeshore cryogenic probe-station, T_{min}=8K, equipped with a 2T superconducting magnet. A small ($\sim 1\mu$A) constant current is applied between S and D (Fig.2a) by using a two-channel Agilent B2912A source-measure unit (SMU). The longitudinal and transverse voltage drops are measured with an Agilent 34420 low-noise nanovoltmeter. Thermoelectrical and other offset voltages are eliminated by measuring each resistance value and inverting the source current in each measurement[58]. Gate biases are applied between the corresponding G and D with the same two-channel SMU (liquid gate) or a Keithley 2410 SMU (back gate). Samples are allowed to degas in vacuum ($< 10^{-5}$mbar) at room T for at least$\sim$ 1h before measurements, in order to remove residual water traces in the electrolyte.

We first characterize the T dependence of the sheet resistance, R_s, under the effect of the liquid top gate. We apply the liquid gate voltage, V_{LG}, at 240K, where the electrolyte is still liquid, and under high-vacuum ($< 10^{-5}$mbar) to minimize unwanted electrochemical interactions and extend the stability window of the ionic liquid[21]. After V_{LG} is applied, we allow the ion dynamics to settle for$\sim$10min before cooling to a base T=2.7K.

Fig.4a plots the T dependence of R_s measured in a four-probe configuration, for different V_{LG} and induced carrier density n_{2d}. Our devices behave similarly to Ref. 23, undergoing first an insulator-to-metal transition near $R_s \sim h/e^2$ at low $n_{2d} < 1 \cdot 10^{13}$cm^{-2}, followed by a metal-to-superconductor transition at high $n_{2d} > 6 \cdot 10^{13}$cm^{-2}. The saturating behavior in the R_s vs T curves in Fig.4a for T $\lesssim$ 50K, close to the insulator-to-metal transition, is typically observed in systems at low n_{2d} characterized by a fluctuating electrostatic potential, such as that due to charged impurities[59]. This applies to ion-gated crystalline systems at low V_{LG}, since the doping is provided by a low density of ions in close proximity to the active channel. These ions induce a perturbation of the local electrostatic potential, locally inducing charge carriers, but are otherwise far apart. The resulting potential landscape is thus inhomogeneous. This low-doping
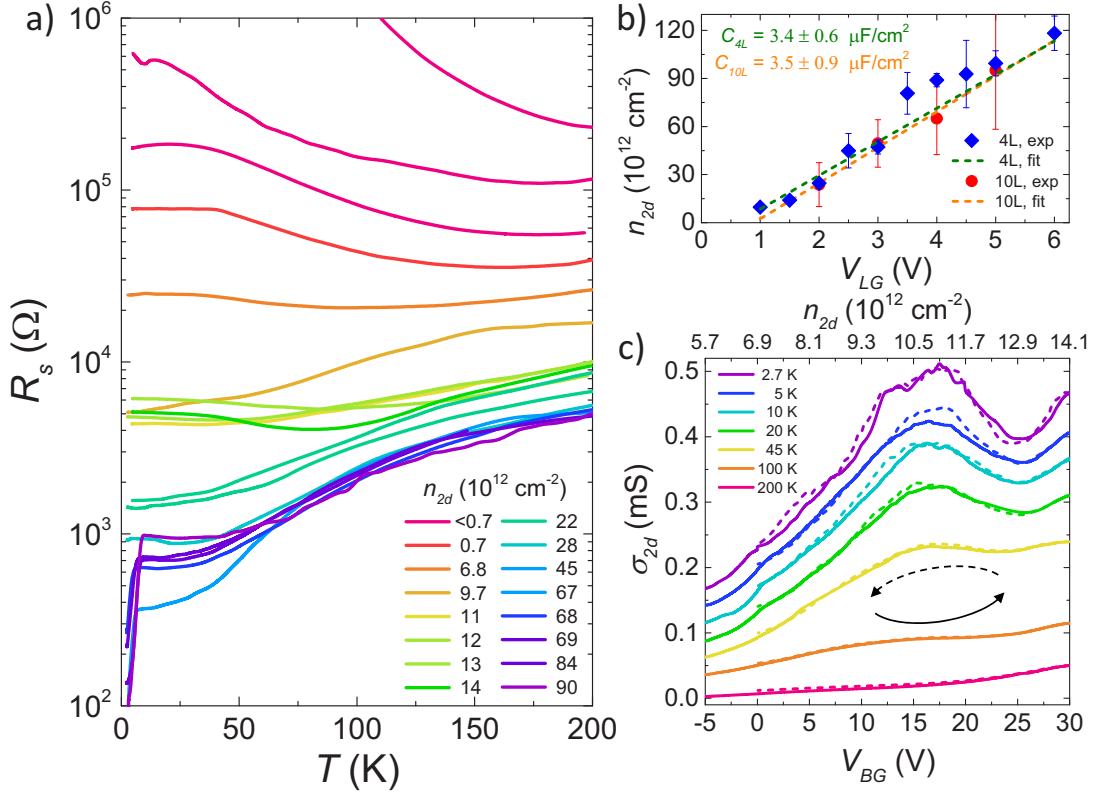
FIG. 4. Transport of dual-gated 4L-MoS$_2$. a) R_s as a function of T for different n_{2d}. b) n_{2d} as function of V_{LG} as determined via Hall effect measurements, for N=4, 10. The liquid gate capacitances are obtained by a linear fit of the data. c) σ_{2d} as a function of V_{BG} at $V_{LG} = 0.9$V, for different T. Each curve is shifted by 3.333×10^{-5}S. The top scale shows the values of n_{2d} estimated from C_{ox}. Solid (dashed) curves are measured for increasing (decreasing) V_{BG}.

($\lesssim 1 \times 10^{13}$cm^{-2}) density inhomogeneity is a known issue in ion-gated crystalline systems, but becomes less and less relevant at higher ionic densities[60]. We employ Hall effect measurements to determine n_{2d} as a function of V_{LG} (see Fig.4b), and, consequently, the liquid gate capacitance C_{LG}. C_{LG} for the BMPPD-TFSI/MoS$_2$ interface ($\sim 3.4 \pm 0.6\mu$F/cm^2) is of the same order of magnitude as for DEME-TFSI/MoS$_2$ in Ref. 61 ($\sim 8.6 \pm 4.1\mu$F/cm^2), where DEME-TFSI is the N,N-Diethyl-N-methyl-N-(2-methoxyethyl)ammonium bis(trifluoromethanesulfonyl)imide ionic liquid[61].

Fig.4a shows that, while for T$\gtrsim$100K R_s is a monotonically decreasing function of n_{2d}, the same does not hold for T$\lesssim$100K, where the various curves cross. In particular, the residual R_s in the normal state R_s^0 (measured just above T_c when the flake is superconducting) varies non-monotonically as a function of n_{2d}. This implies the existence of multiple local maxima in the $R_s^0(n_{2d})$ curve. Consistently with the theoretical predictions of Ref. 46, we find two local maxima. The first and more pronounced occurs when the flake is superconducting, i.e. for $n_{2d} > 6 \cdot 10^{13}$cm^{-2}. This feature was also reported in Refs. 23,31, but not discussed. The second, less pronounced kink, is observed for $1 \cdot 10^{13} \lesssim n_{2d} \lesssim 2 \cdot 10^{13}$cm^{-2}, not previously shown. Both kinks can be seen only for

T$\lesssim$70K and they are smeared for T$\gtrsim$150K.

The kink that emerges in the same range of n_{2d} as the superconducting dome extends across a wide range of V_{LG} ($3 \lesssim V_{LG} \lesssim 6$V) for $n_{2d} \gtrsim 6 \cdot 10^{13}$cm^{-2}, and can be accessed only by LG biasing, due to the small capacitance of the solid BG. This prevents a continuous characterization of its behavior, as n_{2d} induced by LG cannot be altered for $T \lesssim 220$K, as the ions are locked when the electrolyte is frozen. The kink that appears early in the metallic state, on the other hand, extends across a small range of n_{2d} ($1 \lesssim n_{2d} \lesssim 2 \cdot 10^{13}$cm^{-2}), and is ideally suited to be explored continuously by exploiting the dual-gate configuration.

We thus bias our samples in the low-density range of the metallic state ($n_{2d} \sim 7 \cdot 10^{12}$cm^{-2}) by applying $V_{LG} = 0.9$V, and cool the system to 2.7K. We then apply V_{BG} and fine-tune n_{2d} across the kink. We constantly monitor I_{BG} to avoid dielectric breakdown. Fig.4c plots σ_{2d} of a representative device subject to multiple V_{BG} sweeps, as n_{2d} is tuned across the kink. This reproduces well the behavior observed for low V_{LG} ($1 \lesssim n_{2d} \lesssim 2 \cdot 10^{13}$cm^{-2}). The hysteresis between increasing and decreasing V_{BG} is minimal. This kink is suppressed by increasing T, similar to LG gating.

V_{BG} provides us an independent tool to estimate n_{2d}:

If V_{LG} is small enough ($V_{LG} \lesssim 1$V) so that conduction in the channel can be switched off by sufficiently large negative V_{BG} ($V_{BG} \lesssim -25$V), we can write $n_{2d} = C_{ox}/e \cdot (V_{BG} - V_{th})$. Here, $C_{ox} = \epsilon_{ox}/d_{ox}$ is the back gate oxide specific capacitance, $e = 1.602 \cdot 10^{-19}$C is the elementary charge and V_{th} is the threshold voltage required to observe a finite conductivity in the device. We neglect the quantum capacitance C_q of MoS$_2$, since $C_q \gtrsim 100\mu$F/cm$^2 \gg C_{ox}$[16]. By using the dielectric constant of SiO$_2$ ϵ_{ox}=3.9[62] and an oxide thickness $t_{ox} = 90$nm (or $t_{ox} = 285$nm, depending on the experiment) we obtain the n_{2d} scale in the top axis of Fig.4c, in good agreement with the corresponding values in Fig.4a, estimated from the Hall effect measurements in Fig.4b.

The bandstructure of field-effect doped NL-MoS$_2$ depends on N[16] and strain[46]. A fully relaxed N-layer flake, with N≥3, has been predicted to behave as follows[16,46]: For small doping ($x \lesssim 0.05$e$^-$/unit cell, Figs.1b and 5a) only the two spin-orbit split sub-bands at K/K' are populated. At intermediate doping ($0.05 \lesssim x \lesssim 0.1$ e$^-$/unit cell, Figs.1c and 5b), E_F crosses the first spin-orbit split sub-band at Q/Q' (labeled Q$_1$). For large doping ($x \gtrsim 0.1$ e$^-$/unit cell, Figs.1d and 5c) E_F crosses the second sub-band (Q$_2$) and both valleys become highly populated[16]. Even larger doping ($x \gtrsim 0.35$ e$^-$/unit cell) eventually shifts the K/K' valleys above E_F[16].

When E_F crosses these high-energy sub-bands at Q/Q', sharp kinks are expected to appear in the transconductance of gated FL-MoS$_2$[46] (see Fig.1e). These are reminiscent of a similar behavior in liquid-gated FL graphene, where their appearance was linked to the opening of interband scattering channels upon the crossing of high-energy sub-bands[63-65]. Even in the absence of energy-dependent scattering, Ref. 46 showed that σ_{2d} can be expressed as:

$$\sigma_{2d} = e^2 \tau \langle v_\parallel^2 \rangle N(E_F) \propto e^2 \langle v_\parallel^2 \rangle \qquad (3)$$

where $\tau \propto N(E_F)^{-1}$ is the average scattering time, and $N(E_F)$ is the density of states (DOS) at E_F. This implies that σ_{2d} is proportional to the average of the squared in-plane velocity $\langle v_\parallel^2 \rangle$ over the FS[46]. Since $\langle v_\parallel^2 \rangle$ linearly increases with n_{2d} and drops sharply as soon as a new band starts to get doped[46], the kinks in σ_{2d} (or, equivalently, R_s) at $T \lesssim 15$K can be used to determine the onset of doping of the sub-bands in the Q/Q' valleys. At T=0, the kink is a sharp drop in σ_{2d}, emerging for the doping value at which E_F crosses the bottom of the next sub-band. This correspondence is lost due to thermal broadening for T>0, leading to a smoother variation in σ_{2d}. If T is sufficiently large the broadening smears out any signature of the kinks, Fig.4. Ref. 46 calculated that, at finite T, the conductivity kinks define a *doping range* where the sub-band crossing occurs (between R_s minimum and maximum, i.e. the *lower* and *upper* bounds of each kink sets the resolution of this approach). Each sub-band crossing starts after the R_s minimum at lower doping, then develops in correspondence of the inflection point, and is complete once the R_s maximum is reached.

We show evidence for this behavior in Fig.5, where we plot T_c (panel d) and R_s^0 (panel e) as a function of n_{2d}. The electric field is applied both in liquid-top-gate (filled dots and dashed line) and dual-gate (solid red line) configurations. For comparable values of n_{2d}, the liquid-gate geometry features larger R_s^0 than back-gated. This difference is due to increased disorder introduced when n_{2d} is modulated via ionic gating[64-68]. Two kinks appear in the n_{2d} dependence of R_s: a low-doping one for $1.5 \cdot 10^{13} \lesssim n_{2d} \lesssim 2 \cdot 10^{13}$cm^{-2}, and a high-doping one for $7 \cdot 10^{13} \lesssim n_{2d} \lesssim 9 \cdot 10^{13}$cm^{-2}. The plot of the SC dome of gated MoS$_2$ on the same n_{2d} scale shows that the low-doping kink appears well before the SC onset, while the second appears immediately after, before the maximum T_c is reached.

These results can be interpreted as follows. When $n_{2d} \lesssim 1 \cdot 10^{13}$cm^{-2}, only the spin-orbit split sub-bands at K/K' are populated, and the FS is composed only by two pockets, Fig.5a. For n_{2d} between~ 1.5 and $2 \cdot 10^{13}$cm^{-2}, E_F crosses the bottom of the Q$_1$ sub-band and two extra pockets appear in the FS at Q/Q'[16,18], Fig.5b. The emergence of these pockets induces a Lifshitz transition, i.e. an abrupt change in the topology of the FS[69]. Once Q$_1$ is populated and E_F is large enough ($n_{2d} \sim 6 \cdot 10^{13}$cm^{-2}), the system becomes superconducting[23,31]. For slightly larger E_F ($7 \cdot 10^{13} \lesssim n_{2d} \lesssim 9 \cdot 10^{13}$cm^{-2}), E_F crosses the bottom of Q$_2$ resulting in a second Lifshitz transition, and other two pockets emerge in the FS at Q/Q'[16], Fig.5c.

We note that the experimentally observed kinks are at different n_{2d} with respect to the theoretical ones for 3L-MoS$_2$[46]. Ref. 46 predicted that for a 1.28% in-plane tensile strain, Q$_1$ and Q$_2$ should be crossed for $n_{2d} \sim 5 \cdot 10^{13}$ and $\sim 1 \cdot 10^{14}$. Since the positions of the sub-band crossings are strongly dependent on strain[46], we estimate the strain in our devices by monitoring the frequency of the E$_{2g}^1$ mode via Raman spectroscopy. Strain can arise due to a mismatch in the thermal expansion coefficients (TECs) of MoS$_2$[72], SiO$_2$ substrate[73] and Au electrodes[74]. Upon cooling, MoS$_2$, SiO$_2$ and Au would normally undergo a contraction. However the flake is also subject to a tensile strain due to TEC mismatch[70]. The strain, ϵ_{MoS_2}, due to the MoS$_2$-SiO$_2$ TEC mismatch is:

$$\epsilon_{MoS_2} = \int_T^{292K} [\alpha_{MoS_2}(T) - \alpha_{SiO_2}(T)]dT \qquad (4)$$

whereas the strain, ϵ_{Au}, due to the Au contacts is:

$$\epsilon_{Au} = \int_T^{292K} [\alpha_{Au}(T) - \alpha_{SiO_2}(T)]dT \qquad (5)$$

ϵ_{MoS_2} and ϵ_{Au} are~0.1% and~0.3% at ~4K, respectively[70].

Any FL-MoS$_2$ on SiO$_2$ will be subject to ϵ_{MoS_2} at low T. When the flake is contacted, an additional contribution is present due to ϵ_{Au}. This can be more reliably estimated performing T-dependent Raman scattering and comparing the spectra for contacted and uncontacted flakes[70,71]. Figs.6a,b show how a T decrease
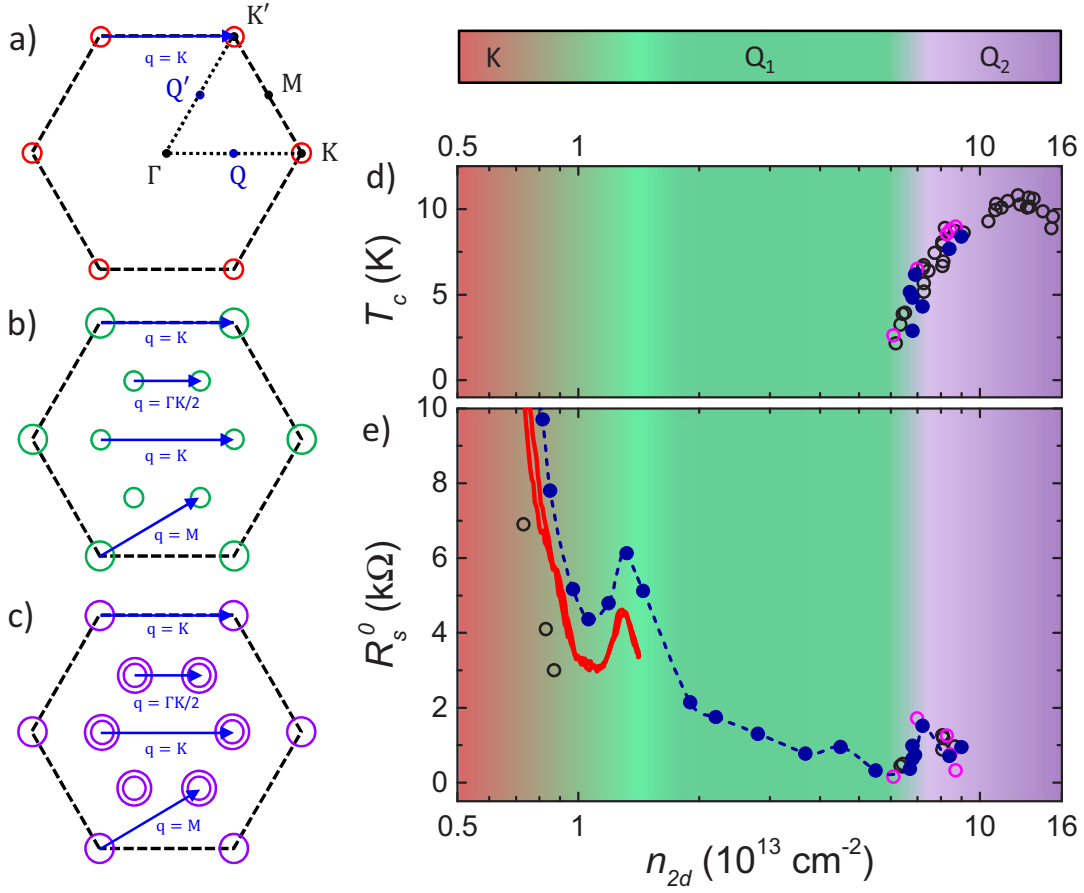
FIG. 5. a-c) Fermi Surface of 3L-MoS$_2$ for the 3 doping values in Fig.1b-d. High symmetry points Γ, M, K, K', and points Q and Q' are shown. Blue arrows indicate representative phonon wave vectors that connect the various FSs. d) SC dome of liquid-gated MoS$_2$ as a function of n$_{2d}$. T_c is determined at 90% of the total transition. e) R_s^0 as a function of n_{2d}, for increasing V_{LG} (blue filled circles) and V_{BG} (solid red line). In d,e), filled circles are our data, black and magenta open circles are taken from Refs. 23,31. The background is color-coded to indicate the doping ranges highlighted in a-c).

results in the E$_{2g}^1$ mode shifting to higher frequencies for both as-prepared and contacted 4L-MoS$_2$, due to anharmonicity[75]. However, in the as-prepared 4L-MoS$_2$, the up-shift is~1cm^{-1} larger with respect to the contacted one. This difference points to a further tensile strain. Refs. 76,77 suggested that uniaxial tensile strain on 1L-MoS$_2$ induces a E$_{2g}^1$ softening and a splitting in two components: E$_{2g}^{1+}$ and E$_{2g}^{1-}$[76,77]. The shift rates for E$_{2g}^{1+}$ and E$_{2g}^{1-}$ are from -0.9 to -1.0cm^{-1}/% and from -4.0 to -4.5cm^{-1}/%, respectively[76,77]. We do not observe splitting, pointing towards a biaxial strain. As for Ref. 71, we calculate a shift rate of E$_{2g}^1$ for biaxial strain from -7.2 to -8.2cm^{-1}/%. The amount of tensile strain on the 4L-MoS$_2$ device can thus be estimated. The E$_{2g}^1$ up-shift difference between contacted and as-prepared 4L-MoS$_2$, ΔPos(E$_{2g}^1$), at 4K is~-1.0cm^{-1}, corresponding to an additional ~0.13% biaxial tensile strain. Thus, assuming a 0.1% strain for the as-prepared 4L-MoS$_2$ due to TEC mismatch with SiO$_2$, we estimate the total strain in the contacted 4L-MoS$_2$ to be~0.23% at~4K.

Fig.7a shows that, for 0.23% tensile strain, the experimentally observed positions of the kinks agree well with a linear extrapolation of the data of Ref. 46 to 4L-MoS$_2$ (representative of our experiments) and for in-plane strain between 0% (bulk) and 1.28% (fully relaxed). These findings indicate that, while the mechanism proposed in Ref. 18 qualitatively describes the general behavior of gated FL-MoS$_2$, quantitative differences arise due to the spin-orbit split of the Q$_1$ and Q$_2$ sub-bands. The main reason for the EPC (and, hence, T_c) increase is the same, i.e. the increase in the number of phonon branches involved in the coupling when the high-energy valleys are populated[18]. However, the finite spin-orbit-split between the sub-bands significantly alters the FS connectivity upon increasing doping[16]. If we consider the relevant phonon wave vectors ($q=\Gamma$,K,M,ΓK/2) for 1L- and FL-MoS$_2$[78,79], and only the K/K' valleys populated, then only phonons near Γ and K can contribute to EPC[18]. The former strongly couple e$^-$ within the same valley[18], but cannot contribute significantly due to the limited size of the Fermi sheets[18]. The latter cou-
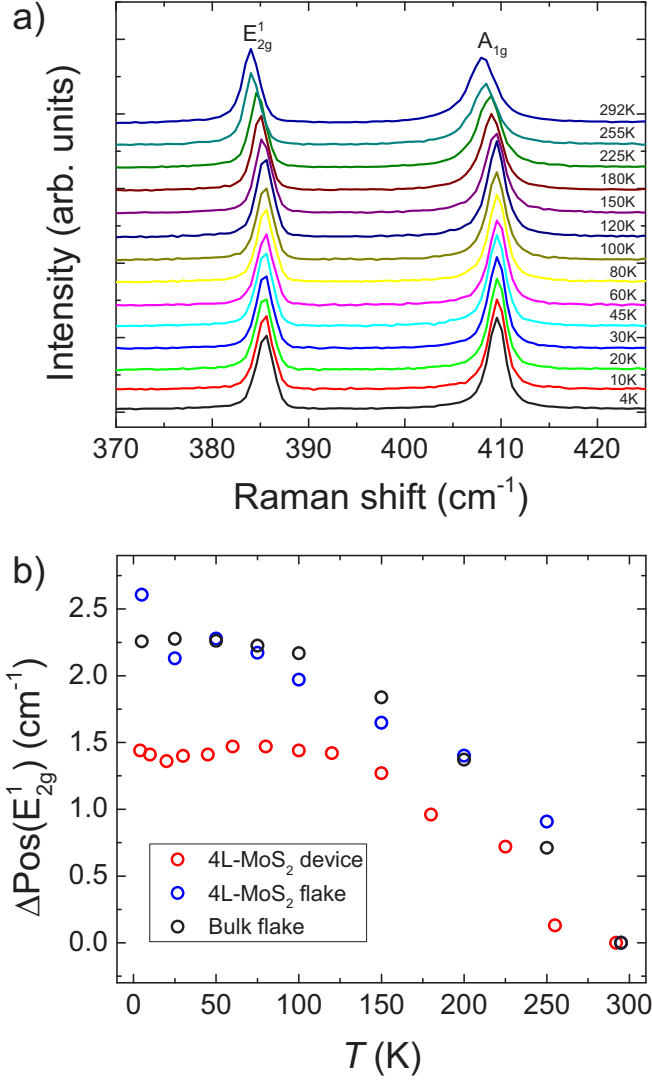
a)

b)

FIG. 6. a) Raman spectra of the 4L-MoS$_2$ device in Fig.2c from 4 to 292K. b) Shift in the position of the E$^1_{2g}$ mode as a function of T for as-prepared bulk flake (black circles), a 4L-MoS$_2$ flake (blue circles), and a 4L-MoS$_2$ device with Au contacts (red circles).
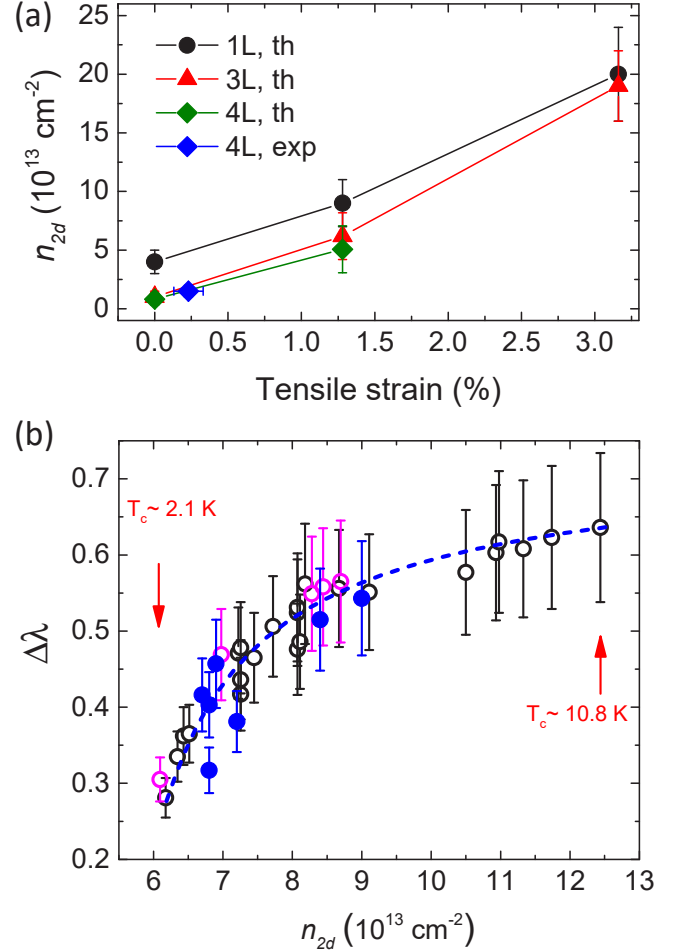

(a)

(b)

FIG. 7. a) Surface carrier densities required to cross the Q$_1$ sub-band in FL-MoS$_2$ as a function of tensile strain. Theoretical values for 1L (black dots and line) and 3L (red triangle and line) from Ref. 46; values for 4L (green diamonds and line) are by linear extrapolation. Blue diamond is the present experiment. b) EPC enhancement due to the crossing of the Q$_2$ sub-band, $\Delta\lambda$, as a function of n_{2d}, assuming $\omega_{ln} = 230 \pm 30$K and $\mu^* = 0.13$[18]. Filled blue circles are our experiments. Black and magenta open circles from Refs. 23,31. The blue dashed line is a guide to the eye.

ple e$^-$ across different valleys[18], and provide a larger contribution[18], insufficient to induce SC. MoS$_2$ flakes are metallic but not superconducting before the crossing of Q$_1$. When this crossing happens, the total EPC increases due to the contribution of longitudinal phonon modes near K[18] (coupling states near two different Q or Q'), near ΓK/2[18] (coupling states near Q to states near Q'), and near M[18] (coupling states near Q or Q' to states near K or K'). However, this first EPC increase associated with Q$_1$ is not sufficient to induce SC, as the SC transition is not observed until immediately before the crossing of the spin-orbit-split sub-band Q$_2$ and the second doping-induced Lifshitz transition. Additionally, the SC dome shows a maximum in the increase of T_c with doping (dT_c/dn_{2d}) across the Q$_2$ crossing, i.e. when a

new FS emerges. Consistently, the subsequent reduction of T_c for $n_{2d} \geq 13 \cdot 10^{13}$cm^{-2} can be associated with the FS shrinkage and disappearance at K/K'[16,18], and might also be promoted by the formation of an incipient Charge Density Wave[80,81] (characterized by periodic modulations of the carrier density coupled to a distortion of the lattice structure[82]).

Since the evolution of the bandstructure with doping is similar in several semiconducting TMDs[16,34,36,45,46], this mechanism is likely not restricted to gated MoS$_2$. The T_c increase in correspondence to a Lifshitz transition is reminiscent of a similar behavior observed in CaFe$_2$As$_2$ under pressure[83], suggesting this may be a general feature across different classes of materials.

We note that the maximum $T_c \sim 11$K is reached at $n_{2d} \simeq 12 \cdot 10^{13}$cm^{-2}, as reported in Ref. 23. This is a doping level larger than any doping level which can be associated with the kink. Thus, the Q_2 sub-band must be highly populated when the maximum T_c is observed. We address this quantitatively with the Allen-Dynes formula[85], which describes the dependence of T_c by a numerical approximation of the Eliashberg theory accurate for materials with a total $\lambda \lesssim 1.5$[85]:

$$T_c(n_{2d}) = \frac{\omega_{ln}}{1.2}\exp\left\{\frac{-1.04\left[1 + \lambda(n_{2d})\right]}{\lambda(n_{2d}) - \mu^*\left[1 + 0.62\lambda(n_{2d})\right]}\right\} \quad (6)$$

where $\lambda(n_{2d})$ is the total EPC as a function of doping, ω_{ln} is the representative phonon frequency and μ^* is the Coulomb pseudo-potential. It is important to evaluate the increase in EPC between the non-superconducting region ($n_{2d} \lesssim 6 \times 10^{13}$cm^{-2}) and the superconducting one, i.e. the enhancement in λ due to the crossing of the sub-band at Q_2. $\Delta\lambda = \lambda(T_c) - \lambda(T_c = 0)$ indicates the EPC increase due to the appearance of e$^-$ pockets at Q_2. By setting $\omega_{ln} = 230 \pm 30$K and $\mu^* = 0.13$ (as for Ref. 18), and using Eq.6, we find that the limit of $\lambda(T_c)$ for $T_c \to 0$ is ~ 0.25. The corresponding $\Delta\lambda$ vs. n_{2d} dependence is shown in Fig.7b. The crossing at Q_2 results in a maximum $\Delta\lambda = 0.63 \pm 0.1$, with a maximum EPC enhancement of $350 \pm 40\%$ with respect to the non-superconducting region. This indicates that the largest contribution to the total EPC, hence to the maximum $T_c \sim 11$K, is associated with the population of the Q_2 sub-band. This is consistent with the reports of a reduced $T_c \sim 2$K in 1L-MoS$_2$[30,48], shown to be superconducting for smaller $n_{2d} \sim 5.5\cdot10^{13}$cm^{-2}[48], hence likely to populate Q_1 only. $n_{2d} \sim 5 \cdot 10^{13}$cm^{-2} is also the doping

expected for the crossing of Q_1 in 1L-MoS$_2$ in presence of a low-T strain similar to that in our 4L-MoS$_2$ devices (see Fig.7a).

In summary, we exploited the large carrier density modulation provided by ionic gating to explore sub-band population and multivalley transport in MoS$_2$ layers. We detected two kinks in the conductivity, associated with the doping-induced crossing of the two sub-bands at Q/Q'. By comparing the emergence of these kinks with the doping dependence of T_c, we showed how superconductivity emerges in gated MoS$_2$ when the Q/Q' valleys are populated, while previous works only considered the filling of K/K'. We highlighted the critical role of the population of the second spin-orbit-split sub-band, Q_2, (and the consequent increase of the FS available for EPC) in the appearance of superconductivity and in the large enhancement of T_c and of EPC in the first half of the superconducting dome. Our findings explain the doping dependence of the SC state at the surface of gated FL-MoS$_2$, and provide a key insight for other semiconducting transition metal dichalcogenides.

* These authors contributed equally to this work.
1 Ferrari, A. C.; Bonaccorso, F.; Fal'ko, V.; Novoselov, K. S.; Roche, S.; Bøggild, P.; Borini, S.; Koppens, F. H.; Palermo, V.; Pugno, N.; Garrido, José A.; Sordan, R.; Bianco, A.; Ballerini, L.; Prato, M.; Lidorikis, E.; Kivioja, J.; Marinelli, C.; Ryhänen; Morpurgo, A. F.; Coleman, J. N.; Nicolosi, V.; Colombo, L.; Fert, A.; Garcia-Hernandez, M.; Bachtold, A.; Schneider, G. F.; Guinea, F.; Dekker, C.; Barbone, M.; Sun, Z.; Galiotis, C.; Grigorenko, A. N.; Konstantatos, G.; Kis, A.; Katsnelson, M.; Vandersypen, L.; Loiseau, A.; Morandi, V.; Neumaier, D.; Treossi, E.; Pellegrini, V.; Polini, M.; Tredicucci, M.; Williams, G. M.; Hong, B. H.; Ahn, J.-H.; Kim, J. M.; Zirath, H.; van Wees, B. J.; van der Zant, H.; Occhipinti, L.; Di Matteo, A.; Kinloch, I. A.; Seyller, T.; Quesnel, E.; Feng, X.; Teo, K.; Rupesinghe, N.; Hakonen, P.; Neil, S. R. T.; Tannock, Q.; Löfwander, T.; Kinaret, J. Science and technology roadmap for graphene, related two-dimensional crystals, and hybrid systems. *Nanoscale* **2015**, *7*, 4598–4810
2 Wang, Q. H.; Kalantar-Zadeh, K.; Kis, A.; Coleman, J. N.; Strano, M. S. Electronics and optoelectronics of two-dimensional transition metal dichalcogenides. *Nature Nan-*

otechnology **2012**, *7*, 699
3 Mak, K. F.; Lee, C.; Hone, J.; Shan, J.; Heinz, T. F. Atomically thin MoS$_2$: a new direct-gap semiconductor. *Physical Review Letters* **2010**, *105*, 136805
4 Splendiani, A.; Sun, L.; Zhang, Y.; Li, T.; Kim, J.; Chim, C.-Y.; Galli, G.; Wang, F. Emerging photoluminescence in monolayer MoS$_2$. *Nano Letters* **2010**, *10*, 1271–1275
5 Mak, K. F.; Shan, J. Photonics and optoelectronics of 2D semiconductor transition metal dichalcogenides. *Nature Photonics* **2016**, *10*, 216
6 Podzorov, V.; Gershenson, M.; Kloc, C.; Zeis, R.; Bucher, E. High-mobility field-effect transistors based on transition metal dichalcogenides. *Applied Physics Letters* **2004**, *84*, 3301–3303
7 Radisavljevic, B.; Radenovic, A.; Brivio, J.; Giacometti, i. V.; Kis, A. Single-layer MoS$_2$ transistors. *Nature Nanotechnology* **2011**, *6*, 147
8 Fang, H.; Chuang, S.; Chang, T. C.; Takei, K.; Takahashi, T.; Javey, A. High-performance single layered WSe$_2$ p-FETs with chemically doped contacts. *Nano Letters* **2012**, *12*, 3788–3792
9 Gourmelon, E.; Lignier, O.; Hadouda, H.; Couturier, G.;

Bernede, J.; Tedd, J.; Pouzet, J.; Salardenne, J. MS$_2$ (M= W, Mo) photosensitive thin films for solar cells. *Solar Energy Materials and Solar Cells* **1997**, *46*, 115–121

[10] Lee, H. S.; Min, S.-W.; Chang, Y.-G.; Park, M. K.; Nam, T.; Kim, H.; Kim, J. H.; Ryu, S.; Im, S. MoS$_2$ nanosheet phototransistors with thickness-modulated optical energy gap. *Nano Letters* **2012**, *12*, 3695–3700

[11] Yin, Z.; Li, H.; Li, H.; Jiang, L.; Shi, Y.; Sun, Y.; Lu, G.; Zhang, Q.; Chen, X.; Zhang, H. Single-layer MoS$_2$ phototransistors. *ACS Nano* **2011**, *6*, 74–80

[12] Koppens, F.; Mueller, T.; Avouris, P.; Ferrari, A.; Vitiello, M.; Polini, M. Photodetectors based on graphene, other two-dimensional materials and hybrid systems. *Nature Nanotechnology* **2014**, *9*, 780

[13] Sun, Z.; Martinez, A.; Wang, F. Optical modulators with 2D layered materials. *Nature Photonics* **2016**, *10*, 227

[14] Carladous, A.; Coratger, R.; Ajustron, F.; Seine, G.; Péchou, R.; Beauvillain, J. Light emission from spectral analysis of Au/MoS$_2$ nanocontacts stimulated by scanning tunneling microscopy. *Physical Review B* **2002**, *66*, 045401

[15] Sundaram, R.; Engel, M.; Lombardo, A.; Krupke, R.; Ferrari, A.; Avouris, P.; Steiner, M. Electroluminescence in single layer MoS$_2$. *Nano Letters* **2013**, *13*, 1416–1421

[16] Brumme, T.; Calandra, M.; Mauri, F. First-principles theory of field-effect doping in transition-metal dichalcogenides: Structural properties, electronic structure, Hall coefficient, and electrical conductivity. *Physical Review B* **2015**, *91*, 155436

[17] Cheiwchanchamnangij, T.; Lambrecht, W. R. Quasiparticle band structure calculation of monolayer, bilayer, and bulk MoS$_2$. *Physical Review B* **2012**, *85*, 205302

[18] Ge, Y.; Liu, A. Y. Phonon-mediated superconductivity in electron-doped single-layer MoS$_2$: a first-principles prediction. *Physical Review B* **2013**, *87*, 241408(R)

[19] Kadantsev, E. S.; Hawrylak, P. Electronic structure of a single MoS$_2$ monolayer. *Solid State Communications* **2012**, *152*, 909–913

[20] Fujimoto, T.; Awaga, K. Electric-double-layer field-effect transistors with ionic liquids. *Physical Chemistry Chemical Physics* **2013**, *15*, 8983–9006

[21] Ueno, K.; Shimotani, H.; Yuan, H.; Ye, J.; Kawasaki, M.; Iwasa, Y. Field-induced superconductivity in electric double layer transistors. *Journal of the Physical Society of Japan* **2014**, *83*, 032001

[22] Saito, Y.; Nojima, T.; Iwasa, Y. Gate-induced superconductivity in two-dimensional atomic crystals. *Superconductor Science and Technology* **2016**, *29*, 093001

[23] Ye, J.; Zhang, Y.; Akashi, R.; Bahramy, M.; Arita, R.; Iwasa, Y. Superconducting dome in a gate-tuned band insulator. *Science* **2012**, *338*, 1193–1196

[24] Braga, D.; Gutierrez Lezama, I.; Berger, H.; Morpurgo, A. F. Quantitative determination of the band gap of WS$_2$ with ambipolar ionic liquid-gated transistors. *Nano Letters* **2012**, *12*, 5218–5223

[25] Yu, Y.; Yang, F.; Lu, X. F.; Yan, Y. J.; Cho, Y.-H.; Ma, L.; Niu, X.; Kim, S.; Son, Y.-W.; Feng, D.; Li, S.; Cheong, S.-W.; Chen, X. H.; Zhang, Y. Gate-tunable phase transitions in thin flakes of 1T-TaS$_2$. *Nature Nanotechnology* **2015**, *10*, 270

[26] Xi, X.; Berger, H.; Forró, L.; Shan, J.; Mak, K. F. Gate Tuning of Electronic Phase Transitions in Two-Dimensional NbSe$_2$. *Physical Review Letters* **2016**, *117*, 106801

[27] Chakraborty, B.; Bera, A.; Muthu, D.; Bhowmick, S.; Waghmare, U. V.; Sood, A. Symmetry-dependent phonon renormalization in monolayer MoS$_2$ transistor. *Physical Review B* **2012**, *85*, 161403

[28] Das, A.; Pisana, S.; Chakraborty, B.; Piscanec, S.; Saha, S.; Waghmare, U.; Novoselov, K.; Krishnamurthy, H.; Geim, A.; Ferrari, A.; Sood, A. K. Monitoring dopants by Raman scattering in an electrochemically top-gated graphene transistor. *Nature Nanotechnology* **2008**, *3*, 210

[29] Das, A.; Chakraborty, B.; Piscanec, S.; Pisana, S.; Sood, A.; Ferrari, A. Phonon renormalization in doped bilayer graphene. *Physical Review B* **2009**, *79*, 155417

[30] Costanzo, D.; Jo, S.; Berger, H.; Morpurgo, A. F. Gate-induced superconductivity in atomically thin MoS$_2$ crystals. *Nature Nanotechnology* **2016**, *11*, 339

[31] Lu, J.; Zheliuk, O.; Leermakers, I.; Yuan, N. F.; Zeitler, U.; Law, K. T.; Ye, J. Evidence for two-dimensional Ising superconductivity in gated MoS$_2$. *Science* **2015**, *350*, 1353–1357

[32] Saito, Y.; Nakamura, Y.; Bahramy, M. S.; Kohama, Y.; Ye, J.; Kasahara, Y.; Nakagawa, Y.; Onga, M.; Tokunaga, M.; Nojima, T.; Yanase, Y.; Iwasa, Y. Superconductivity protected by spin-valley locking in ion-gated MoS$_2$. *Nature Physics* **2016**, *12*, 144–149

[33] Chen, Q.; Lu, J.; Liang, L.; Zheliuk, O.; Ali, A.; Sheng, P.; Ye, J. Inducing and Manipulating Heteroelectronic States in a Single MoS$_2$ Thin Flake. *Physical Review Letters* **2017**, *119*, 147002

[34] Wu, Z.; Xu, S.; Lu, H.; Khamoshi, A.; Liu, G.-B.; Han, T.; Wu, Y.; Lin, J.; Long, G.; He, Y.; Cai, Y.; Yao, Y.; Zhang, F.; Wang, N. Even–odd layer-dependent magneto-transport of high-mobility Q-valley electrons in transition metal disulfides. *Nature Communications* **2016**, *7*, 12955

[35] Roldán, R.; Cappelluti, E.; Guinea, F. Interactions and superconductivity in heavily doped MoS$_2$. *Physical Review B* **2013**, *88*, 054515

[36] Das, T.; Dolui, K. Superconducting dome in MoS$_2$ and TiSe$_2$ generated by quasiparticle-phonon coupling. *Physical Review B* **2015**, *91*, 094510

[37] Kormányos, A.; Zólyomi, V.; Drummond, N. D.; Rakyta, P.; Burkard, G.; Fal'ko, V. I. Monolayer MoS$_2$: trigonal warping, the Γ valley, and spin-orbit coupling effects. *Physical Review B* **2013**, *88*, 045416

[38] Yuan, N. F.; Mak, K. F.; Law, K. Possible topological superconducting phases of MoS$_2$. *Physical Review Letters* **2014**, *113*, 097001

[39] Costanzo, D.; Zhang, H.; Reddy, B. A.; Berger, H.; Morpurgo, A. F. Tunnelling spectroscopy of gate-induced superconductivity in MoS$_2$. *Nature Nanotechnology* **2018** DOI:10.1038/s41565-018-0122-2

[40] Hsu, Y.-T.; Vaezi, A.; Fischer, M. H.; Kim, E.-A. Topological superconductivity in monolayer transition metal dichalcogenides. *Nature Communications* **2017**, *8*, 14985

[41] Nakamura, Y.; Yanase, Y. Odd-parity superconductivity in bilayer transition metal dichalcogenides. *Physical Review B* **2017**, *96*, 054501

[42] Lu, J. M.; Zheliuk, O.; Chen, Q.; Leermakers, I.; Hussey, N. E.; Zeitler, U.; Ye, J. T. Full superconducting dome of strong Ising protection in gated monolayer WS$_2$. *Proceedings of the National Academy of Sciences of the United States of America* **2018** *115*, 3551

[43] de la Barrera, S. C.; Sinko, M. R.; Gopalan, D. P.; Sivadas, N.; Seyler, K. L.; Watanabe, K.; Taniguchi, T.; Tsen, A. W.; Xu, X.; Xiao, D.; Hunt, B. M. Tuning Ising superconductivity with layer and spin-orbit coupling in

two-dimensional transition-metal dichalcogenides. *Nature Communications* **2018** *9*, 1427

[44] Cui, X.; Lee, G.-H.; Kim, Y. D.; Arefe, G.; Huang, P. Y.; Lee, C.-H.; Chenet, D. A.; Zhang, X.; Wang, L.; Ye, F.; Pizzocchero, F.; Jessen, B. S.; Watanabe, K.; Taniguchi, T.; Muller, D. A.; Low, T.; Kim, P.; Hone, J. Multi-terminal transport measurements of MoS_2 using a van der Waals heterostructure device platform. *Nature Nanotechnology* **2015**, *10*, 534

[45] Kang, M.; Kim, B.; Ryu, S. H.; Jung, S. W.; Kim, J.; Moreschini, L.; Jozwiak, C.; Rotenberg, E.; Bostwick, A.; Kim, K. S. Universal mechanism of band-gap engineering in transition-metal dichalcogenides. *Nano Letters* **2017**, *17*, 1610–1615

[46] Brumme, T.; Calandra, M.; Mauri, F. Determination of scattering time and of valley occupation in transition-metal dichalcogenides doped by field effect. *Physical Review B* **2016**, *93*, 081407(R)

[47] Pickett, W. E. *Emergent Phenomena in Correlated Matter*; Forschungszentrum Jülich GmbH and Institute for Advanced Simulations: Jülich, Germany, 2013

[48] Fu, Y.; Liu, E.; Yuan, H.; Tang, P.; Lian, B.; Xu, G.; Zeng, J.; Chen, Z.; Wang, Y.; Zhou, W.; Xu, K.; Gao, A.; Pan, C.; Wang, M.; Wang, B.; Zhang, S.-C.; Hwang, H. Y.; Miao, F. Gated tuned superconductivity and phonon softening in monolayer and bilayer MoS_2. *npj Quantum Materials* **2017**, *2*, 52

[49] Novoselov, K.; Jiang, D.; Schedin, F.; Booth, T.; Khotkevich, V.; Morozov, S.; Geim, A. Two-dimensional atomic crystals. *Proceedings of the National Academy of Sciences of the United States of America* **2005**, *102*, 10451–10453

[50] Casiraghi, C.; Hartschuh, A.; Lidorikis, E.; Qian, H.; Harutyunyan, H.; Gokus, T.; Novoselov, K.; Ferrari, A. Rayleigh imaging of graphene and graphene layers. *Nano Letters* **2007**, *7*, 2711–2717

[51] Kutz, M. *Handbook of Materials Selection*; John Wiley & Sons, 2002

[52] Stacy, A.; Hodul, D. Raman spectra of IVB and VIB transition metal disulfides using laser energies near the absorption edges. *Journal of Physics and Chemistry of Solids* **1985**, *46*, 405–409

[53] Verble, J.; Wieting, T. Lattice Mode Degeneracy in MoS_2 and Other Layer Compounds. *Physical Review Letters* **1970**, *25*, 362

[54] Wieting, T.; Verble, J. Infrared and Raman Studies of Long-Wavelength Optical Phonons in Hexagonal MoS_2. *Physical Review B* **1971**, *3*, 4286

[55] Lee, C.; Yan, H.; Brus, L. E.; Heinz, T. F.; Hone, J.; Ryu, S. Anomalous lattice vibrations of single-and few-layer MoS_2. *ACS Nano* **2010**, *4*, 2695–2700

[56] Zhang, X.; Han, W.; Wu, J.; Milana, S.; Lu, Y.; Li, Q.; Ferrari, A.; Tan, P. Raman spectroscopy of shear and layer breathing modes in multilayer MoS_2. *Physical Review B* **2013**, *87*, 115413

[57] Tan, P.; Han, W.; Zhao, W.; Wu, Z.; Chang, K.; Wang, H.; Wang, Y.; Bonini, N.; Marzari, N.; Pugno, N.; Savini, G.; Lombardo, A.; Ferrari, A. C. The shear mode of multilayer graphene. *Nature Materials* **2012**, *11*, 294

[58] Daghero, D.; Paolucci, F.; Sola, A.; Tortello, M.; Ummarino, G.; Agosto, M.; Gonnelli, R.; Nair, J. R.; Gerbaldi, C. Large conductance modulation of gold thin films by huge charge injection via electrochemical gating. *Physical Review Letters* **2012**, *108*, 066807

[59] Zabrodskii, A. G; Zinoveva, K. N. Low-temperature conductivity and metal-insulator transition in compensate n-Ge. *Journal of Experimental and Theoretical Physics* **1984**, *59*, 425

[60] Ren, Y.; Yuan, H.; Wu, X.; Chen, Z.; Iwasa, Y.; Cui, Y.; Hwang, H. Y.; Lai, K. Direct Imaging of Nanoscale Conductance Evolution in Ion-Gel-Gated Oxide Transistors. *Nano Letters* **2015** *15*, 4730

[61] Shi, W.; Ye, J.; Zhang, Y.; Suzuki, R.; Yoshida, M.; Miyazaki, J.; Inoue, N.; Saito, Y.; Iwasa, Y. Superconductivity series in transition metal dichalcogenides by ionic gating. *Scientific Reports* **2015**, *5*, 12534

[62] El-Kareh, B. *Fundamentals of Semiconductor Processing Technologies*; Kluwer Academic Publishers, 1995

[63] Ye, J.; Craciun, M. F.; Koshino, M.; Russo, S.; Inoue, S.; Yuan, H.; Shimotani, H.; Morpurgo, A. F.; Iwasa, Y. Accessing the transport properties of graphene and its multilayers at high carrier density. *Proceedings of the National Academy of Sciences* **2011**, *108*, 13002–13006

[64] Gonnelli, R.; Piatti, E.; Sola, A.; Tortello, M.; Dolcini, F.; Galasso, S.; Nair, J. R.; Gerbaldi, C.; Cappelluti, E.; Bruna, M.; Ferrari, A. Weak localization in electric-double-layer gated few-layer graphene. *2D Materials* **2017**, *4*, 035006

[65] Piatti, E.; Galasso, S.; Tortello, M.; Nair, J. R.; Gerbaldi, C.; Bruna, M.; Borini, S.; Daghero, D.; Gonnelli, R. Carrier mobility and scattering lifetime in electric double-layer gated few-layer graphene. *Applied Surface Science* **2017**, *395*, 37–41

[66] Piatti, E.; Chen, Q.; Ye, J. Strong dopant dependence of electric transport in ion-gated MoS_2. *Applied Physics Letters* **2017**, *111*, 013106

[67] Gallagher, P.; Lee, M.; Petach, T. A.; Stanwyck, S. W.; Williams, J. R.; Watanabe, K.; Taniguchi, T.; Goldhaber-Gordon, D. A high-mobility electronic system at an electrolyte-gated oxide surface. *Nature Communications* **2015**, *6*, 6437

[68] Ovchinnikov, D.; Gargiulo, F.; Allain, A.; Pasquier, D. J.; Dumcenco, D.; Ho, C.-H.; Yazyev, O. V.; Kis, A. Disorder engineering and conductivity dome in ReS_2 with electrolyte gating. *Nature Communications* **2016**, *7*, 12391

[69] Lifshitz, I. Anomalies of electron characteristics of a metal in the high pressure region. *Sov. Phys. JETP* **1960**, *11*, 1130–1135

[70] Yoon, D.; Son, Y.-W.; Cheong, H. Negative thermal expansion coefficient of graphene measured by Raman spectroscopy. *Nano Letters* **2011**, *11*, 3227–3231

[71] Mohiuddin, T.; Lombardo, A.; Nair, R.; Bonetti, A.; Savini, G.; Jalil, R.; Bonini, N.; Basko, D.; Galiotis, C.; Marzari, N.; Pugno, N.; Savini, G.; Lombardo, A.; Ferrari, A. C. Uniaxial strain in graphene by Raman spectroscopy: G peak splitting, Grüneisen parameters, and sample orientation. *Physical Review B* **2009**, *79*, 205433

[72] Gan, C. K.; Liu, Y. Y. F. Direct calculation of the linear thermal expansion coefficients of MoS_2 via symmetry-preserving deformations. *Physical Review B* **2016**, *94*, 134303

[73] *Standard Reference Material 739 Certificate*; National Institute of Standards and Technology: Gaithersburg, MD, 1991

[74] Nix, F.; MacNair, D. The thermal expansion of pure metals: copper, gold, aluminum, nickel, and iron. *Physical Review* **1941**, *60*, 597

[75] Klemens, P. Anharmonic decay of optical phonons. *Physical Review* **1966**, *148*, 845

[76] Lee, J.-U.; Woo, S.; Park, J.; Park, H.; Son, Y.-W.; Cheong, H. Strain-shear coupling in bilayer MoS_2. *Nature Communications* **2017**, *8*, 1370

[77] Conley, H. J.; Wang, B.; Ziegler, J. I.; Haglund Jr, R. F.; Pantelides, S. T.; Bolotin, K. I. Bandgap engineering of strained monolayer and bilayer MoS_2. *Nano Letters* **2013**, *13*, 3626–3630

[78] Molina-Sanchez, A.; Wirtz, L. Phonons in single-layer and few-layer MoS_2 and WS_2. *Physical Review B* **2011**, *84*, 155413

[79] Ataca, C.; Topsakal, M.; Akturk, E.; Ciraci, S. A comparative study of lattice dynamics of three-and two-dimensional MoS_2. *The Journal of Physical Chemistry C* **2011**, *115*, 16354–16361

[80] Rösner, M.; Haas, S.; Wehling, T. Phase diagram of electron-doped dichalcogenides. *Physical Review B* **2014**, *90*, 245105

[81] Piatti, E.; Chen, Q.; Tortello, M.; Ye, J. T.; Gonnelli, R. S. Possible charge-density-wave signatures in the anomalous resistivity of Li-intercalated multilayer MoS_2. arXiv:1802.08449

[82] Gor'kov, L. P.; Grüner, G. *Charge Density Waves In Solids*, 1st ed.; Elsevier: North Holland, 1989; Vol. 25

[83] Gonnelli, R. S.; Daghero, D.; Tortello, M.; Ummarino, G. A.; Bukowski, Z.; Karpinski, J.; Reuvekamp, P. G.; Kremer, R. K.; Profeta, G.; Suzuki, K.; Kuroki, K. Fermi-Surface topological phase transition and horizontal Order-Parameter nodes in $CaFe_2As_2$ under pressure. *Scientific Reports* **2016**, *6*, 26394

[84] Innocenti, D.; Poccia, N.; Ricci, A.; Valletta, A.; Caprara, S.; Perali, A.; Bianconi, A. Resonant and crossover phenomena in a multiband superconductor: Tuning the chemical potential near a band edge. *Physical Review B* **2010**, *82*, 184528

[85] Allen, P. B.; Dynes, R. Transition temperature of strong-coupled superconductors reanalyzed. *Physical Review B* **1975**, *12*, 905

[86] Giannozzi, P.; Andreussi, O.; Brumme, T.; Bunau, O.; Buongiorno Nardelli, M.; Calandra, M.; Car, R.; Cavazzoni, C.; Ceresoli, D.; Cococcioni, M.; Colonna, N.; Carnimeo, I.; Dal Corso, A.; de Gironcoli, S.; Delugas, P.; DiStasio Jr, R. A.; Ferretti, A.; Floris, A.; Fratesi, G.; Fugallo, G.; Gebauer, R.; Gerstmann, U.; Giustino, F.; Gorni, T.; Jia, J.; Kawamura, M.; Ko, H.-Y.; Kokalj, A.; Küçükbenli, E.; Lazzeri, M.; Marsili, M.; Marzari, N.; Mauri, F.; Nguyen, N. L.; Nguyen, H.-V.; Otero-de-la-Roza, A.; Paulatto, L.; Poncé, S.; Rocca, D.; Sabatini, R.; Santra, B.; Schlipf, M.; Seitsonen, A. P.; Smogunov, A.; Timrov, I.; Thonhauser, T.; Umari, P.; Vast, N.; Wu, X.; Baroni, S. Advanced capabilities for materials modelling with quantum espresso. *Journal of Physics: Condensed Matter* **2017** *29*, 465901

[87] Brumme, T.; Calandra, M.; Mauri, F. Electrochemical doping of few-layer ZrNCl from first principles: Electronic and structural properties in field-effect configuration. *Physical Review B* **2014** *89*, 245406